# Curved crystal x-ray optics for monochromatic imaging with a clinical source

Ayhan Bingölbali and C. A. MacDonald[a)]
*Department of Physics, University at Albany, SUNY, Albany, New York 12222*

(Received 22 July 2008; revised 29 December 2008; accepted for publication 23 January 2009; published 12 March 2009)

Monochromatic x-ray imaging has been shown to increase contrast and reduce dose relative to conventional broadband imaging. However, clinical sources with very narrow energy bandwidth tend to have limited intensity and field of view. In this study, focused fan beam monochromatic radiation was obtained using doubly curved monochromator crystals. While these optics have been in use for microanalysis at synchrotron facilities for some time, this work is the first investigation of the potential application of curved crystal optics to clinical sources for medical imaging. The optics could be used with a variety of clinical sources for monochromatic slot scan imaging. The intensity was assessed and the resolution of the focused beam was measured using a knife-edge technique. A simulation model was developed and comparisons to the measured resolution were performed to verify the accuracy of the simulation to predict resolution for different conventional sources. A simple geometrical calculation was also developed. The measured, simulated, and calculated resolutions agreed well. Adequate resolution and intensity for mammography were predicted for appropriate source/optic combinations. © *2009 American Association of Physicists in Medicine*. [DOI: 10.1118/1.3083568]

Key words: monochromatic, mammography, x-ray optics, curved crystal

## I. INTRODUCTION

Mammography is the primary screening tool for the detection of breast cancer; however, false positives cause unnecessary trauma and false negatives cause critical delays in treatment. Using modeling[1] and synchrotron,[2,3] or other research sources,[4,5] monochromatic beam mammography has been shown to increase contrast and reduce dose relative to conventional broadband imaging. Broadband sources subject the patient to a range of photon energies around the ideal energy. The lower energy x rays do not penetrate tissue very effectively, contributing to patient dose without providing enough signal intensity to create a high quality, low noise image. Higher energy x rays, on the other hand, penetrate too well, causing poor subject contrast and increased x-ray scattering, which further degrades the image contrast. A single crystal monochromator can be used to diffract the characteristic x-ray peak from a clinical x-ray source to produce a very narrow energy bandwidth beam. Monochromators use diffraction from single crystals to select a narrow wavelength range from a broadband source. The incident x-ray beam must be near the right angle and energy to be diffracted according to Bragg's law,[6]

$$\lambda = 2d \sin \theta, \tag{1}$$

where $\lambda$ is the x-ray wavelength, $d$ is the crystal plane spacing, and $\theta$ is the angle between the x-ray beam and the crystal surface. For a flat crystal, the majority of the incident radiation hits at an angle outside of the narrow acceptance bandwidth of the crystal and is lost, as shown in Fig. 1. The resulting low intensity would cause unacceptable motion blur. This can be obviated by using crystals with large acceptance bandwidths, but that results in poor resolution.[7,8] Research sources such as synchrotrons have adequately high intensity to be used with small bandwidth monochromators but are generally unavailable for clinical use.[3] Another technique to provide a more monochromatic beam from a clinical source is to use a pair of thick absorption filters to select a limited range of photon energies.[9,10] This has the disadvantage of limiting the tube voltage, since, unlike the case when a crystal monochromator is employed, increasing tube voltages harden the beam and broaden its bandwidth. Thus the loss of intensity due to the limited transmission through the thick filters must be compensated by higher currents, which can cause tube loading or spot size issues. Further, the beam remains relatively broadband compared to the output from a monochromator crystal. Narrow bandwidth monochromatic beams also allow clinical access to high contrast techniques such as diffraction enhanced imaging (DEI) and coherent diffraction imaging.[11,12]

An alternative solution to providing sufficient monochromatic beam intensity from a conventional x-ray tube is the use of curved monochromator crystals, like that pictured in Fig. 2. Doubly curved crystals (DCCs) collect and focus the incident beam from a large solid angle as shown in Fig. 3.[13–18] This leads to the desired increase in intensity in the monochromatic beam. However, the resolution resulting from the focused beam must be carefully assessed.

One cause of resolution loss in imaging is geometric blur due to the angular divergence of the incident beam, sketched for the no-optic case in Fig. 4. The blur is given by

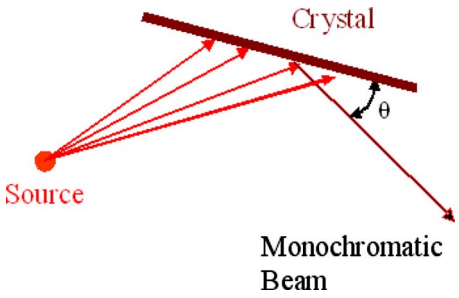



FIG. 1. Diffraction from a flat monochromator crystal, which selects only a narrow range of angles from the beam and so gives low intensity from a clinical source.

$$\text{blur} \sim \alpha D, \tag{2}$$

where the angular divergence $\alpha$ is taken as the range of angles incident at a single point. For example, for the no-optic case the local divergence is[19]

$$\alpha \approx \frac{\text{source size}}{\text{source-to-object distance}}. \tag{3}$$

To provide 50 $\mu$m (10 line pairs/mm) resolution in a 50 mm thick breast, the angular resolution must be better than 1 mrad. For focusing optics, the angular divergence near the focal point can be much larger than this and may become as large as the global divergence, i.e., the optic size divided by the focal length. Away from the focal point, the local divergence is dependent on the detailed geometry of the x-ray beam. Measurements and simulations of local divergence and resolution were performed.

### I.A. Doubly curved crystal x-ray optics

DCC x-ray optics are designed so that all rays incident from the source hit the optic at the Bragg angle and then focus to the focal point, as shown in Fig. 3. This requires that the source $S$ optic and focal point $F$ are located on a Rowland circle of radius $R$ while the in-plane radius of curvature of the optic is $2R$. In three dimensions, the optic surface is a toroid with a radius of curvature $2R \sin^2 \theta$ in the out-of-plane direction.[20] $R$ is related to the optic focal length,[20] the optimal source-to-optic distance, by $f=2R \sin \theta$. Since DCC optics collect and focus x rays from a large solid angle, they make more efficient use of a conventional x-ray tube. The DCC optic used in this work was from X-ray Optical Systems, Inc. (East Greenbush, NY), serial number A723, designed for the $K\alpha_1$ energy (17.478 keV) of a molybdenum x-ray source. The parameters of the optic are listed in Table I.




FIG. 2. Curved monochromator crystal. The crystal is toroidal, curved in both the vertical and horizontal directions. This optic had only one column with only three crystal segments. An optimized optic would be both wider and taller, containing more segments in each column and multiple staggered columns.

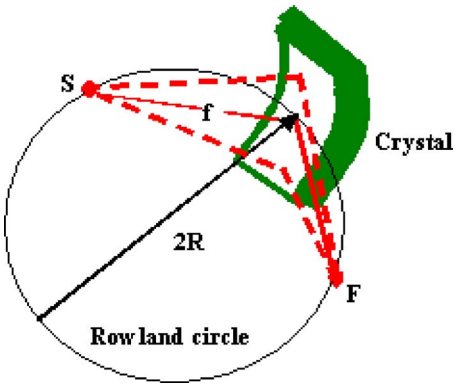



FIG. 3. Geometry of diffraction for toroidal crystals. The crystal surface is at the correct angle over its whole surface for diffraction from the source. The dashed lines represent the rays which are out of the plane of the Rowland circle.

## II. METHODS

### II.A. Measurements

An Oxford ultrabright low power (10 W at 25 kV) molybdenum source was employed in this study. The source diameter was measured to be $100 \pm 10$ $\mu$m using pinhole images at a series of source distances.[21] The low power source allows for convenient optic testing; a higher power source would be required for clinical imaging. A higher power source would typically have a larger spot size. As discussed in Secs. III A and V, this would require a larger focal length and longer optic-to-patient distance to maintain high resolution.

The optic, source, and detector were aligned using a robust DCC optics alignment system.[21,22] The measurement setup is shown in Fig. 5.

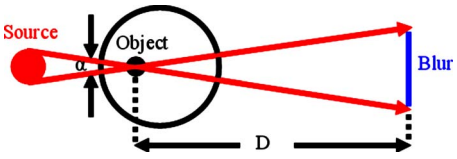



FIG. 4. The geometry of a finite point source and resulting image blur. $D$ is the object-to-detector distance.

TABLE I. Parameters of the DCC optic. The optic used silicon (220) diffraction, which gives a Bragg angle of 10.646° at 17.478 keV, for which λ=0.709 Å.

| DCC optic | Focal distance $f$ (mm) | Optic size (mm$^2$) | Input angular width | In-plane bending radius (mm) | Out-of-plane bending radius (mm) |
|---|---|---|---|---|---|
| A723 | 190 | 11.5×45 | 0.63°×13.37° | 1028 | 35 |

### II.A.1. Intensity

The diffracted intensity after the optic was measured with a high purity germanium (HPGe) detector manufactured by Canberra Industries, Inc., Meriden, CT.

### II.A.2. Resolution

The basic setup of the measurements using the x-ray source, curved crystal optic, and computed radiography (CR) detector is shown in Fig. 5. The CR detector was a Fuji (Valhalla, NY) restimuble phosphor computed radiography plate read with Fuji bioimaging analyzer BAS-1800 with 50 $\mu$m pixels.

An image of the beam after the optic is shown in Fig. 6. The divisions between the three crystal segments of the optic shown in the photograph of Fig. 2 can be seen in the x-ray image. An optic optimized for imaging would have additional columns of segments, with the divisions staggered so that a scanned beam would not have missing rows of intensity. Optics with large numbers of segments are commonly produced for x-ray fluorescence applications.[23] For resolution measurements a tungsten knife edge[24,25,8] was mounted on horizontal and vertical translation stages and placed between the optic and a Fuji image plate as shown in Fig. 5. The knife edge was aligned to block roughly half of diffracted beam. Images were taken at series of distances $D$ from the knife edge and for different optic-to-knife distances $L$. The images were converted to intensity profiles with Fuji IMAGE GAUGE software. From the profile/MW mode in that program, the lane profile tool was selected. This tool is used to connect two points with a lane of set width and measure the integrated intensity along the lane. The width of the lane was set at 5 pixels for both knife edge and no-knife images. The lane was started at approximately the same initial point on the knife edge and no-knife images. To remove the effect of intensity variation across the field, the ratio of the knife edge to the no-knife profiles was taken. Registration was performed manually by shifting the knife-edge profile laterally to align prominent features. The ratio was then normalized to account for variability in sensitivity between plates, and the resulting edge response function was analyzed.[26] Because of the low source power, the data were too noisy to compute the derivative line spread function. Instead, the edge response was fitted directly to

$$g(x) = C + A\frac{1}{\sigma\sqrt{\pi}}\int_{-\infty}^{x} e^{-((x-x_o)/\sigma)^2}dx = \frac{1}{2}\left[1 + \mathrm{erf}\left(\frac{x-x_o}{\sigma}\right)\right], \quad (4)$$

where $A$ is the height, $C$ is the offset, $x_o$ is the position of the center of the peak, $\sigma$ is the Gaussian width, and erf is the error function, normalized so that erf(+∞)=1. $A$, $C$, $\sigma$, and $x_o$ were adjusted to give the best fit in Excel software to obtain $\sigma$ and thus the FWHM=$2\sigma\sqrt{\ln(2)}$. The modulation transfer function (MTF) of the entire imaging chain was not computed to avoid detector specific results, as the intent was to

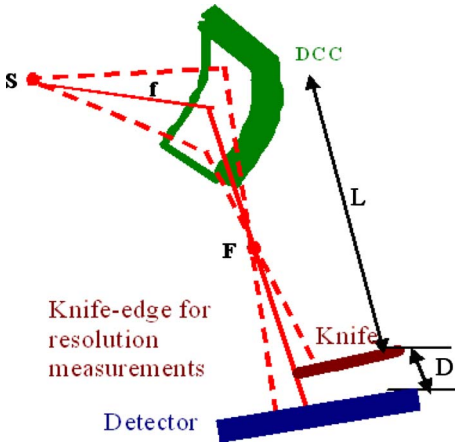



FIG. 5. Monochromatic imaging setup for intensity and resolution measurements with the DCC optic. For the intensity measurements, a HPGe detector was used with no knife. The resolution measurements were performed with a CR detector.

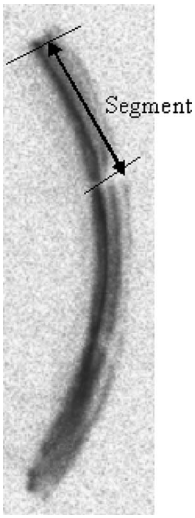



FIG. 6. The diffracted output image taken 300 mm from the optic.

assess the effects of the source-optic pair independent of the choice of detector.

The net resolution of the optics was given by subtracting the resolution of the detector in quadrature from the measured value,[8] $\sigma=\sqrt{\sigma^2_{\text{measured}}-\sigma^2_{\text{detector}}}$. In general the blur, measured at large optic-to-detector distances, was much greater than the 50 $\mu$m pixel size of the detector, so the correction had negligible effect. The large detector distances allowed for accurate measurement of the optics angular divergence independent of the detector resolution.

### II.B. Simulation model

A Monte Carlo simulation model was developed in order to assess the optic resolution.[21,22] Comparisons to measured resolutions were performed to assess the ability of the simulation to predict resolutions for different source-optic-detector geometries. The simulation was based on simple ray tracing, similar to that used in SHADOW.[27,28] The finite source was modeled by stepping an ideal point source across the actual source area. Photons were emitted from the source in triplets, two at the $K\alpha_1$ energy and one at the $K\alpha_2$ energy. The photons were diffracted with a Gaussian probability according to their angle of incidence and the measured angular acceptance width of the crystal. More details of the simulation have been discussed elsewhere.[21,22]

For the horizontal resolution studies, a simulated "knife" was placed on the optic output axis. Photons incident on the knife half-plane were discarded. The remaining photons were propagated to the detector. To compare the simulated resolution profile with the measured images from the CR detector, simulated locations at the detector plane were binned into 50 $\mu$m wide pixels. The matrix of intensity per pixel was input to Excel for analysis. Since the width of the lane was 5 pixels for the measured resolutions, five rows (or five columns for vertical resolution) at the center of the image were summed to give a horizontal profile. The FWHM was found using the Excel code fitting as for the experimental data or, because the simulated data were less noisy than the measured data, simply as the width from 11% to 89% of the normalized intensity of the simulated knife-edge profiles. The two values arise from Eq. (4), since $g(x_o+\text{FWHM}/2)=0.89$ and $g(x_o-\text{FWHM}/2)=0.11$.

## III. RESULTS

### III.A. Intensity

The total measured monochromatic photon emission rate from the optic, measured with the detector near the focal point so that the entire beam was collected, was $3.9\times10^5$ photons/s with a 0.012 kW Mo source operated at 24 kV and 0.5 mA with optic A723. The tested optic was an experimental model with a poor efficiency of 2%.[21] Using a large 10 kW source at 50 kV and 200 mA and a commercial optic with five columns of crystal segments, a longer focal length, and a more typical 20% efficiency would yield a flux of $2\times10^{11}$ photons/s, which is sufficient to cover a $10\times20$ cm$^2$ field for mammography with the required[29]

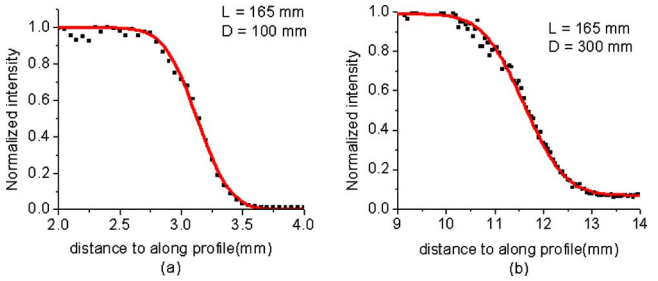



FIG. 7. Vertical resolution profiles with the knife edge 165 mm from the optic, 25 mm before the focal point. The image plate distance was 100 mm for (a) and 300 mm for (b). The horizontal axis is the distance along the profile from an arbitrary point on the image. The solid line is from Eq. (4), with the best fit $A$, $C$, $\sigma$, and $x_o$.

$10^9$ photons/cm$^2$ in 1 s. The optic size and efficiency affect required source power but do not affect dose, as the optic would be placed before the patient. Also, the optic selects only the $K\alpha$ characteristic line, so increasing the tube voltage does not change the output spectrum but increases the flux by a factor of 25.[30] As discussed in Sec. V, the larger spot size of the more powerful source would require larger optic-to-patient and source-to-optic distances to maintain high resolution. The optics would not be affected by heating issues at these distances. Any position instability in the source spot of the high power tube would not affect the output, so long as it remained within the design source diameter, as discussed in Sec. V.

### III.B. Resolution

Typical measured normalized intensity profiles across the knife edge are shown in Fig. 7. The resultant measured resolutions for two knife positions near the focal point are shown in Fig. 8 for a series of detector-to-knife-edge distances $D$. For fixed knife positions, as the detector-to-knife distance is increased the size of the blur increases, but the angular divergence, $\alpha=2\tan^{-1}(\text{blur}/2D)$, decreases slightly, as shown in Fig. 9. The measured horizontal resolutions are quite similar to the vertical resolutions at these distances and the Monte Carlo simulations are in good agreement with the measurements. As expected, the angular divergences are unacceptably high for knife positions such as these, which are near the focal point. The geometrical calculation to estimate resolutions is discussed in the next section.

The remainder of the measurements at different knife-edge distances was made with an image plate distance of 300 mm. The results are shown in Fig. 10. The resolution improved when the knife edge was placed farther from the focal point.

## IV. GEOMETRICAL CALCULATION OF RESOLUTION

The simulation analysis is computationally slow. Greater efficiency and better understanding can be provided by a simple geometrical analysis. The simulation results indicated that the major contribution to the blur was the finite source size. This was modeled by regarding the focal point as a

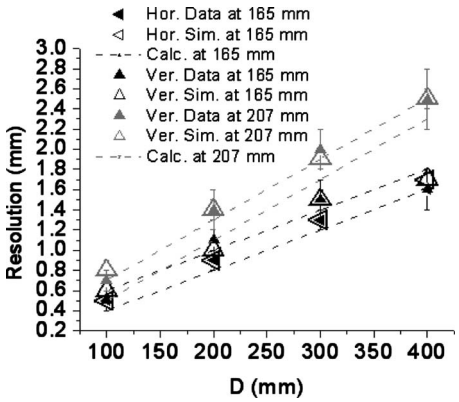



FIG. 8. Measured, simulated, and calculated resolutions when the knife edge was 165 (black) and 207 mm (gray) from the optic (corresponding to 25 before or 17 mm after the focal point). The dashed lines represent the range of values calculated from the geometry discussed in Sec. IV. The open symbols are values from the simulation, and the closed symbols are data.

simple source to compute the geometric blur in the usual fashion, as shown in Fig. 11. Thus, the blur is given by

$$\text{blur} = \text{width} \times \frac{D}{P}, \tag{5}$$

where $D$ is the distance between the knife edge and the detector and $P$ is the distance from the focal point to the knife edge, $P=|L-f|$ where $f$ is the focal distance and $L$ is the distance between the optic and the knife edge. At first it would seem that the appropriate parameter for the "width" would simply be the measured size of the focal spot, in analogy with the no-optic case sketched in Fig. 4. However, unlike a simple point source, the direction that the ray leaves the focal spot is correlated with its position, as shown in Figs. 12 and 13. Using the full width of the focal spot, which was $274\times335$ $\mu\text{m}^2$, overestimates the blur. A reasonable fit to the simulation results, as shown Fig. 14, is found if the source diameter $s$ is used for the width in Eq. (5). This corresponds to the usual case in the absence of the optic but taking the focal spot as an intermediate relay between the finite source and the blur after the optic.

The agreement between calculation, simulation, and measurement, as shown in Figs. 8 and 10, allows for rapid calculation for different optic and system geometries. The dashed lines in Figs. 8 and 10 represent a range of values from Eq. (5) due to the uncertainty in source size.

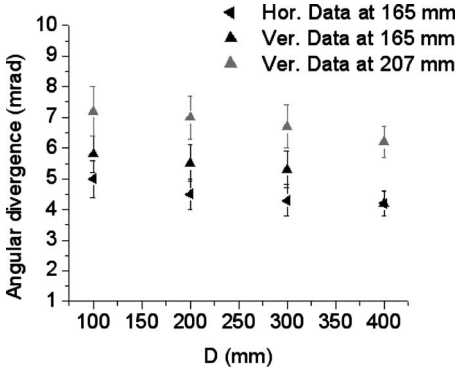



FIG. 9. Measured angular divergences when the knife edge was near the focal point.

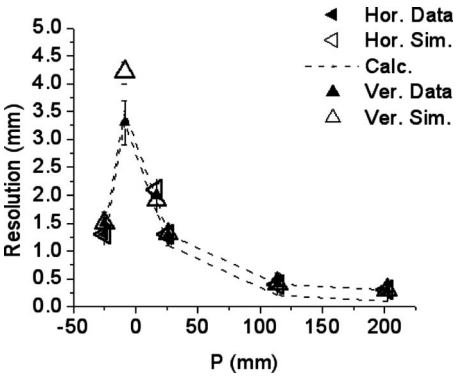



FIG. 10. Measured, simulated, and calculated resolutions as a function of the distance $P$ of the knife from the focal point of the optic. The image plate-to-knife-edge distance was 300 mm. The dashed lines represent the range of values calculated from the geometry discussed in Sec. IV.

If the knife edge is located before the focal point, as shown in Fig. 15, the blur would be given by

$$\text{blur} = \text{width} \times \frac{D+P}{P} \approx s\frac{D+P}{P}, \tag{6}$$

where $D$ is the distance between the focal point and the detector, $P$ is the distance from the focal point to the knife edge, $P=|L-f|$, and $s$ is the source diameter. This formula was used for the distances before the focal spot in Figs. 8 and 10.

## V. OPTIMIZATION FOR MAMMOGRAPHY

Several considerations affect the choice of optic focal length $f$, optic-to-object distance $L$, object-to-detector distance $D$, and source diameter $s$. For objects placed before the focal point, as in Fig. 15, the image size can be larger or smaller than the object, as shown in Fig. 16. Demagnifying or magnifying can be useful depending on the detector type.

Table II shows the simulated and calculated resolutions for objects placed before the focal point at constant $L=25$ mm and $D=50$ mm for different focal length optics. The calculated results agree with the simulated resolutions, verifying the basic geometry. The horizontal and vertical simulations give similar results. The results at a fixed focal point-to-object distance, $P=|L-f|$, are independent of $f$, as shown in Table III. However, since the blur in Eq. (6) can

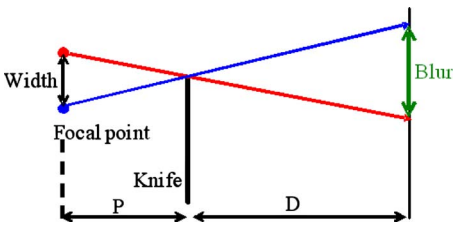



FIG. 11. Geometry for the DCC optic resolution when the knife edge is located beyond the focal point.

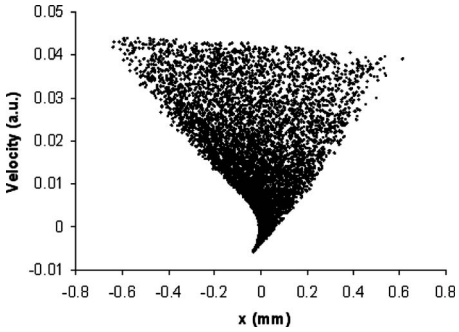



FIG. 12. Simulated normalized horizontal component of ray velocity versus its horizontal position at the focal point. While rays near $x=0$ can move away with a large range of possible directions, rays near the edges of the focal spot, e.g., for $x=0.5$ mm, can only move away in small range of directions, e.g., only with a large positive $x$ component of velocity.

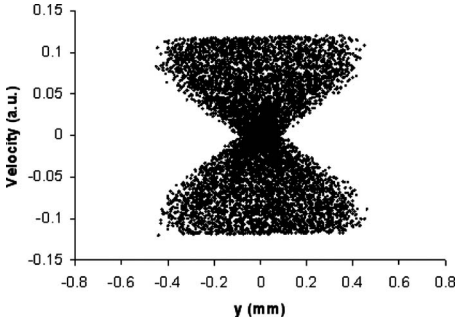



FIG. 13. Simulated normalized vertical ray velocity versus vertical position at the focal point. Rays near the edges of the focal spot can only move away in directions far from the optic axis.

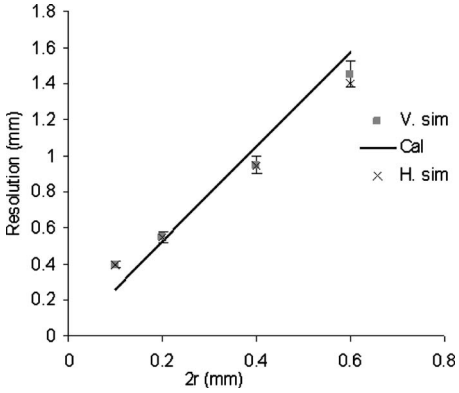



FIG. 14. Simulated resolution as a function of source diameter, $s=2r$, using a focal length of $f=190$ mm, a knife distance of $L=304$ mm, and an image plate distance of $D=300$ mm. The solid line is Eq. (5), with the source diameter used for the width.

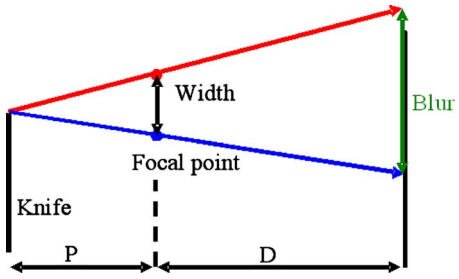



FIG. 15. Geometry for the DCC optic resolution when the knife edge is located before the focal point.

never be smaller than the source diameter, small source spots are required, as shown in Table IV. Small focal spots would require low power sources and therefore long exposure times. As a result, placing the patient after the focal point would be more suitable for mammography.

For objects at a fixed distance $P$ after the optic, the resolution becomes poor if the patient-to-detector distance $D$ is increased, even with a small source diameter, as shown in Table V. This expected from Eq. (5) and was as seen in the measurements in Fig. 8. Thus a small $D$ is desired, as for conventional no-optic systems. For mammography, the minimum distance of $D$ is 50 mm due to patient thickness. Therefore, for the rest of the simulated and calculated resolutions, $D$ was taken as 50 mm.

The calculated resolution is given at constant optic-to-patient distance $L=700$ mm for various focal length optics in Table VI. The resolution is better if the object is far from the focal point, since $P=|L-f|$ is then large. As the available detector had 50 $\mu$m pixels, the predicted high resolution for the $f=190$ mm case could not be directly verified by measurement although the source size was set to the experimental value. However, the measured angular divergence for large values of $P$ was small and in good agreement with the simulations and geometrical calculations.

Increasing the spot size to a more typical value of 0.3 mm would require an optic-to-patient distance $P$ of 500 mm to provide an adequate resolution of 30 $\mu$m ($\sim$17 line pairs/mm). Because the optic has a measured acceptance bandwidth of 0.05°,[22] a source size of 0.3 mm would require focal length of 340 mm for the entire source to be efficiently utilized by the optic. Thicker optics or ones made of materials with natural mosaicity have large acceptance angles and so would not require as long a focal length.[22]

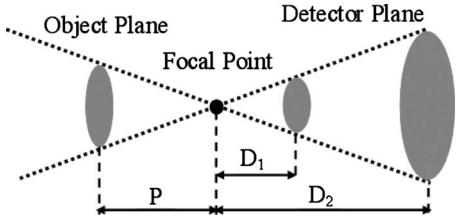



FIG. 16. Geometric magnification or demagnification is possible when the patient is placed between the optic and focal point.

TABLE II. Simulated and calculated resolutions for detector distance $D=50$ mm with the patient placed before the focal point as in Fig. 16. The optic-to-patient distance is $L=25$ mm. The resolution is poor if $f \sim L$. The source diameter was $s=0.1$ mm.

| $f$ (mm) | Horizontal simulation (mm) | Vertical simulation (mm) | Calculation (mm) |
|---|---|---|---|
| 50 | $0.20 \pm 0.05$ | $0.25 \pm 0.05$ | 0.30 |
| 190 | $0.15 \pm 0.05$ | $0.15 \pm 0.05$ | 0.13 |
| 500 | $0.10 \pm 0.05$ | $0.10 \pm 0.05$ | 0.11 |
| 650 | $0.10 \pm 0.05$ | $0.15 \pm 0.05$ | 0.11 |

TABLE III. Simulated and calculated resolutions for $D=50$ mm, with the patient placed at $P=-175$ mm before the focal point. The source diameter was $s=0.1$ mm.

| $f$ (mm) | $L$ (mm) | Horizontal simulation (mm) | Vertical simulation (mm) | Calculation (mm) |
|---|---|---|---|---|
| 190 | 15 | $0.10 \pm 0.05$ | $0.15 \pm 0.05$ | 0.13 |
| 500 | 325 | $0.10 \pm 0.05$ | $0.15 \pm 0.05$ | 0.13 |
| 650 | 475 | $0.10 \pm 0.05$ | $0.15 \pm 0.05$ | 0.13 |

TABLE IV. Simulated and calculated resolutions for a detector distance $D=50$ mm with the patient at $P=-175$ mm before the focal point with a 190 mm focal length optic.

| Source diameter (mm) | Simulation (mm) | Calculation (mm) |
|---|---|---|
| 0.05 | $0.10 \pm 0.05$ | 0.07 |
| 0.1 | $0.15 \pm 0.05$ | 0.13 |
| 0.2 | $0.25 \pm 0.05$ | 0.26 |

TABLE V. Simulated and calculated vertical resolutions become poor even with the patient after the focal point when $D$ is increased. $f=500$ mm with $L=1020$ mm. The source diameter was $s=0.1$ mm.

| $D$ (mm) | Simulation (mm) | Calculation (mm) |
|---|---|---|
| 100 | $0.05 \pm 0.05$ | 0.02 |
| 300 | $0.05 \pm 0.05$ | 0.06 |
| 500 | $0.1 \pm 0.05$ | 0.1 |
| 1000 | $0.2 \pm 0.05$ | 0.2 |

TABLE VI. Calculated resolution with patient thickness $D=50$ mm and optic-to-patient distance $L$ of 700 mm. The resolution is poor if the object is close to the focal point, if $f \sim L$. The source diameter was $s=0.1$ mm.

| $P$ (mm) | $f$ (mm) | Calculation (mm) |
|---|---|---|
| 650 | 50 | 0.008 |
| 510 | 190 | 0.01 |
| 200 | 500 | 0.03 |
| 50 | 650 | 0.1 |

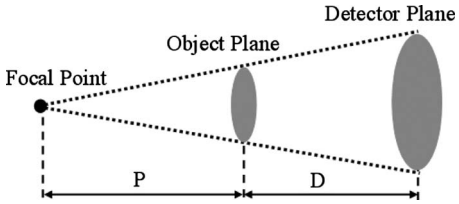



FIG. 17. The geometric magnification when the patient is placed beyond the focal point. The magnification changes between the object entrance at $P$ and the exit plane at $D+P$.

Varying $P$ also changes the differential magnification. The magnification ranges from 1 to $(D+P)/P$ depending on the depth of the object within the patient, as shown in Fig. 17. Thus, using a large value of $P$ also avoids large differential magnification.

Another important factor in choosing object distance is field of view (FOV). A vertical FOV of 100 mm would allow one-dimensional scanning, similar to a conventional slot scan system. The horizontal width of the beam for the optic used in the measurement was $11.5 \sin \theta = 2.1$ mm. This could be increased by using multiple columns of optic segments to allow for a wider slot. From the geometry of Fig. 18, the vertical field of view is given by

$$\mathrm{FOV} = \mathrm{CS}\frac{P}{f}, \tag{7}$$

where CS is the vertical crystal size and $P$ is the focal point-to-object distance. Since the maximum crystal size is proportional to the radius of curvature, which is proportional to the focal length,[20] the FOV is determined solely by $P$. A large value of $P$ then also provides a large field of view. For example, using the measured case of $f=190$ mm and a 45 mm crystal height, $P$ must be larger than 422 mm to have a FOV larger than 100 mm.

Setting the patient thickness to $D=50$ mm and a focal point to patient distance of $P=500$ mm gives a resolution of 17 line pairs/mm for a 0.3 mm diameter source, a field of view of 118 mm, and a maximum differential magnification of 100%–110%. All of these parameters are independent of the focal length of the optic, although efficient utilization of a large source requires a focal length of at least 340 mm. Above this value, because the size of the optic scales with focal length, intensity also depends only on the number of segments and the optic efficiency but not on the focal length. However, smaller focal length optics would allow for shorter overall distances from source to detector, so a more compact system.

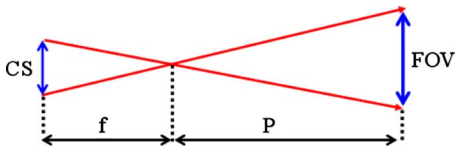



FIG. 18. Field of view. CS is the crystal size, $P$ is the focal point to object distance, and $f$ is the focal length.

## VI. CONCLUSION

DCC optics have a large collection area, so intense monochromatic beams can be produced using a conventional x-ray tube. Measured resolutions were in good agreement with a Monte Carlo simulation and a simple geometrical calculation. Adequately small angular divergences were measured for large optic-to-object distances. Adequate resolution, intensity, and FOV and small differential magnification were predicted for patients placed more than 50 cm beyond the focal point of the optics with typical conventional sources.

## ACKNOWLEDGMENTS

The authors would like to acknowledge X-ray Optical Systems, Inc. for supplying the optic and funding from the DOD Breast Cancer Research Project under Contract Nos. DMD170210517, W81XWH04107, and W81XWH0610667.

[a]Electronic mail: c.macdonald@albany.edu.

[1]J. M. Boone and J. A. Seibert, "A comparison of mono- and polyenergetic x-ray beam performance for radiographic and fluoroscopic imaging," Med. Phys. **21**, 1853–1863 (1994).
[2]R. E. Johnston, D. Washburn, E. Pisano, C. Burns, W. C. Thomlinson, L. D. Chapman, F. Arfelli, N. F. Gmur, Z. Zhong, and D. Sayers, "Mammographic phantom studies with synchrotron radiation," Radiology **200**, 659–663 (1996).
[3]P. Suortti and W. Thonlinson, "Medical applications of synchrotron radiation," Phys. Med. Biol. **48**, R1–R35 (2003).
[4]R. Fairchild, H. L. Atkins, E. Lebowitz, and D. Greenberg, "Investigation of I-125 as an isotopic source for mammography," Invest. Radiol. **10**, 511–518 (1975).
[5]A. Krol, A. Ikhlef, J. C. Kieffer, D. A. Bassano, C. C. Chamberlain, Z. Jiang, H. Pepin, and S. C. Prasad, "Laser-based microfocused x-ray source for mammography: Feasibility study," Med. Phys. **24**, 725–732 (1997).
[6]W. H. Bragg and W. L. Bragg, "The reflection of x-rays by crystals," Proc. R. Soc. London, Ser. A **88**, 428–438 (1913); "The reflection of x-rays by crystals. II.," **89**, 246–248 (1913).
[7]M. Gambaccini, A. Tuffanelli, A. Taibi, A. Fantini, and A. Del Guerra, "A Bragg diffraction based quasi-monochromatic source for mammography using mosaic crystals," Proc. SPIE **3770**, 174–184 (1999).
[8]F. R. Sugiro, D. Li, and C. A. MacDonald, "Beam collimation with polycapillary x-ray optics for high contrast high resolution monochromatic imaging," Med. Phys. **31**, 3288–3297 (2004).
[9]R. J. Jennings, P. W. Queen, R. M. Gagne, and T. R. Fewell, "Evaluation of x-ray sources for mammography," Proc. SPIE **1896**, 259–268 (1993).
[10]R. Fahrig and M. J. Yaffe, "Optimization of spectral shape in digital mammography: Dependence on anode material, breast thickness, and lesion type," Med. Phys. **21**, 1473–1481 (1994).
[11]A. Y. Nikulin, A. V. Darahanau, R. Horney, and T. Ishikawa"High-resolution X-ray diffraction imaging of non-Bragg diffracting materials using phase retrieval X-ray diffractometry (PRXRD) technique," Physica B: Condensed Matter **349**, 281–295 (2004).
[12]E. D. Pisano, R. E. Johnston, D. Chapman, J. Geradts, M. V. Iacocca, C. A. Livasy, D. B. Washburn, D. E. Sayers, Z. Zhong, M. Z. Kiss, and W. C. Thomlinson, "Human breast cancer specimens: Diffraction-enhanced imaging with histologic correlation-improved conspicuity of lesion detail compared with digital radiography," Radiology **214**, 895–901 (2000).
[13]P. Siddons, in *Crystal Monochromators and Bent Crystals*," in Handbook of Optics edited by M. Bass (McGraw-Hill, New York, 2000), Vol. III, Chap. 22, pp. 22.1–22.7.
[14]D. W. Berreman, J. Stamatoff, and S. J. Kennedy, "Doubly curved crystal point-focusing x-ray monochromators: Geometrical and practical optics," Appl. Opt. **16**, 2081–2085 (1977).
[15]D. W. Berreman, "Dynamical theory x-ray diffraction in flat, focusing, and distorted crystals by Abelés's matrix method," Phys. Rev. B **14**, 4313–4317 (1976).
[16]H. H. Johann, "Die Erzeugung lichtstarker Röntgenspektren mit Hilfe von Konkavkristallen," Z. Phys. A **69**, 185–206 (1931).
[17]D. B. Wittry and D. M. Golijanin, "Large aperture point-focusing diffractor for x-rays," Appl. Phys. Lett. **52**, 1381–1382 (1988).
[18]D. B. Wittry and S. Sun, "X-ray optics of doubly curved diffractors," J. Appl. Phys. **67**, 1633–1638 (1990).
[19]J. T. Bushberg, J. A. Seibert, E. M. Leidholdt, Jr., and J. M. Boone, *The Essential Physics of Medical Imaging*, 2nd ed. (Lippincott, Philadelphia, 2002).
[20]D. W. Berreman, "Single quartz crystal point focusing x-ray monochromator," Rev. Sci. Instrum. **26**, 1048–1052 (1955).
[21]A. Bingölbali, Ph.D. thesis, University at Albany, State University of New York, 2008.
[22]A. Bingölbali and C. A. MacDonald, "Quality assessment system for curved crystal x-ray optics," Nucl. Instrum. Methods Phys. Res. B **267**, 832–841 (2009)
[23]Z. W. Chen, W. M. Gibson, and H. Huang, "High definition x-ray fluorescence: principles and techniques," X-Ray Optics and Instrumentation Volume 2008 (http://www.hindawi.com/GetArticle.aspx?doi=10.1155/2008/318171).
[24]J. A. Trail and R. L. Byer, "Compact scanning soft-x-ray microscope using a laser-produced plasma source and normal-incidence multilayer mirrors," Opt. Lett. **14**, 539–541 (1989).
[25]Y. Iketaki, Y. Horikawa, K. Nagai, S. Mochimaru, Y. Ohta, H. Kamijou, and M. Shibuya, "Measurement of knife-edge responses of a Schwarzschild x-ray objective," Jpn. J. Appl. Phys., Part 1 **32**, 1837–1841 (1993).
[26]D. G. Kruger, C. C. Abreu, E. G. Hendee, A. Kocharian, W. W. Peppler, C. A. Mistretta, and C. A. MacDonald, "Imaging characteristics of x-ray capillary optics in digital mammography," Med. Phys. **23**, 187–196 (1996).
[27]B. Lai and F. Cerrina, "Shadow: A synchrotron radiation ray tracing program," Nucl. Instrum. Methods Phys. Res. A **246**, 337–341 (1986).
[28]M. Sánchez del Río and R. J. Defus, "XOP 2.1–A new version of the x-ray optics software toolkit," AIP Conf. Proc. **705**, 784–787 (2004).
[29]J. Freudenberger, E. Hell, and W. Knupfer, "Perspectives of medical x-ray imaging," Nucl. Instrum. Methods Phys. Res. A **466**, 99–104 (2001); "Erratum to: 'Perspectives of medical x-ray imaging," Nucl Instrum. Methods Phys. Res. A **474**, 295 (2001).
[30]J. B. Ullrich and C. A. MacDonald, in *Electron Impact Sources*, in Handbook of Optics, edited by M. Bass (McGraw-Hill, New York, 2000), Vol. III, Chap. 31, pp. 31.5–31.9.